Aerospace Science and Technology 172 (2026) 111693

Contents lists available at ScienceDirect

Aerospace Science and Technology

journal homepage: www.elsevier.com/locate/aescte

Drag modulation strategy for small satellites aerocapture on mars

Valerio Orlandini [a,*], Renato Paciorri [a], Aldo Bonfiglioli [b]

[a] Department of mechanical and aerospace engineering, University of Rome La Sapienza, Via Eudossiana 18, Rome, 00184, Lazio, ItalyItaly
[b] School of engineering, University of Basilicata, Via Nazario Sauro 85, Potenza, 85100, Basilicata, Italy

ARTICLE INFO

Editor: Dr Qu Qiulin

Keywords:
Aerocapture
HIAD
Fluid-structure interaction
Hypersonic flows
Inflatable structures

ABSTRACT

This paper presents a novel approach to the aerocapture maneuver for SmallSat missions to Mars. One of the main challenges preventing the use of aerocapture in interplanetary missions is the uncertainty in atmospheric density, which arises from inaccuracies in atmospheric models or the occurrence of natural events. The proposed approach addresses this issue through a continuous drag modulation technique, which mitigates or eliminates the effects of unexpected density variations during atmospheric flight relative to the nominal density distribution.

Specifically, continuous drag modulation is achieved by leveraging the ability of inflatable shields to alter their shape by adjusting the inflation pressure. Variations in atmospheric density that could cause deviations from the nominal maneuver are counteracted by corresponding adjustments in the shield's shape, induced by changes in inflation pressure. Finally, the paper includes a preliminary discussion on the inflation system that enables this continuous drag modulation.

1. Introduction

Small Satellite (SmallSat) devices differ from traditional satellites due to their lightweight design, with a mass of no more than 180 kg [1]. This makes them a cost-effective solution for various applications, including satellite constellations for signal transmission, space exploration, planetary missions, and the economical testing of larger prototypes.

To further enhance the cost-effectiveness of these innovative devices, recent studies have explored the use of the aerocapture maneuver to position SmallSats in orbit around celestial bodies beyond Earth [2,3]. The aerocapture maneuver leverages aerodynamic drag to slow down the incoming probe, allowing it to enter orbit around a target planet. By minimizing reliance on the propulsion system during orbital insertion, this technique conserves propellant, ultimately enabling a larger payload capacity.

Orlandini et al. [4] estimated that, for Mars, the aerocapture maneuver leads to an increase in payload capacity between 700% and 1,500%. The benefits of aerocapture are even more significant for Titan, where mass savings can reach nearly 1,700% compared to aerobraking for an arrival speed 8 km/s [5]. Consequently, the aerocapture maneuver enables mission planning to other planets at a significantly lower cost than traditional propulsion-based orbit insertions.

However, the primary challenge of this maneuver is the potential for unexpected variations in the atmospheric density profile compared to the one assumed during the design phase, which can affect the vehicle's trajectory during atmospheric re-entry. This is best explained by reference to the drag formula:

$$D = \frac{1}{2}\rho_\infty U_\infty^2 C_D A \tag{1}$$

where D is the aerodynamic drag, ρ_∞ is the atmospheric density at the flight altitude, U_∞ is the spacecraft velocity, A its cross-sectional area and C_D is the drag coefficient, which depends upon the vehicle's shape.

For example, underestimating the actual atmospheric density results in a stronger drag force on the spacecraft, causing greater deceleration. This can lead to a lower orbit than intended or even a crash on the planet's surface. In contrast, overestimating density results in less deceleration than expected, which can place the spacecraft in a higher orbit [6] or, if its velocity exceeds the planet's escape velocity, prevent it from being captured altogether.

Currently, errors and uncertainties in atmospheric model data can cause significant deviations in the predicted density profile during an aerocapture maneuver. For example, NASA's Global Reference Atmospheric Model (GRAM) [7] has an error margin of approximately ±20% when estimating atmospheric density for Mars at altitudes relevant to aerocapture [8]. When assessing aerocapture on Neptune and Titan using the Neptune-GRAM [9] and Titan-GRAM [10] models, Lockman et al. [11,12] report uncertainty ranges of -70% to +239% for Neptune and -44% to +65.5% for Titan. These uncertainties stem primarily from an incomplete understanding of planetary atmospheres due to limited data availability. For instance, the Neptune model relies solely on data from the Voyager mission, whereas the Titan model incorporates

---

[*] Corresponding author.
E-mail address: valerio.orlandini@uniroma1.it (V. Orlandini).

https://doi.org/10.1016/j.ast.2026.111693
Received 17 September 2025; Received in revised form 9 January 2026; Accepted 9 January 2026

data from both the Voyager and Cassini-Huygens missions. Furthermore, transient phenomena such as solar activity and dust storms on Mars can cause temporary discrepancies between the actual density distribution and the values predicted by atmospheric models.

Two techniques have been proposed in the literature to compensate for unexpected atmospheric density variations: lift modulation [13] and drag modulation [14]. Lift modulation involves adjusting the spacecraft's lift-to-drag ratio by altering its attitude or shape during the aerocapture maneuver. This allows the spacecraft to control aerodynamic forces and successfully complete the maneuver, even in the presence of unpredictable density fluctuations during re-entry.

Drag modulation, on the other hand, works by modifying the vehicle's drag coefficient and cross-sectional area to counteract the effects of unexpected density changes on drag. As described in Eq. (1), this is achieved by altering the spacecraft's shape to adjust the product $C_D A$ while maintaining the designed aerodynamic drag value.

Compared to lift modulation, drag modulation is a simpler technique that enables the use of inflatable heat shields, also known as Hypersonic Inflatable Aerodynamic Decelerators (HIADs). HIADs consist of an inflatable structure covered by a flexible heat shield. They are compactly stowed during launch and deployed by inflation at a specific pressure just before atmospheric entry, forming an aeroshell significantly larger than the launch vehicle's diameter. Unlike rigid heat shields, a deployable HIAD allows for a lower ballistic coefficient, β, for the same payload, reducing both mechanical and thermal loads. HIADs rely on Flexible Thermal Protection System (F-TPS) materials [15], which are specifically designed to withstand extreme temperatures while retaining flexibility.

Several drag modulation techniques have been proposed in the literature, such as those discussed in [14]. The simplest of these is the single-jettison method, where the heat shield is released at a specific point in the trajectory, increasing the ballistic coefficient. While this approach is easy to implement, it lacks precision and does not guarantee a successful aerocapture maneuver, as it cannot compensate for density variations that occur after the shield has been jettisoned.

This work introduces a novel continuous drag modulation technique tailored for SmallSat aerocapture, utilizing HIADs capable of adjusting their cross-sectional area by regulating the internal inflation pressure. Specifically, this method employs a control system that continuously modifies the HIAD inflation pressure to adjust the $C_D A$ value, compensating for atmospheric density variations and ideally maintaining the nominal drag throughout the aerocapture maneuver.

To enable this control process, the system requires an aerodynamic database linking inflation pressure to the corresponding $C_D A$ value at each point along the aerocapture trajectory. To construct this database, we employed an advanced Fluid-Structure Interaction (FSI) modeling approach for HIADs in hypersonic flow. This technique [6,16,17] integrates a shock-fitting Computational Fluid Dynamics (CFD) solver [18–20] with the nonlinear structural solver MSC Nastran [21], providing accurate aerodynamic predictions for the control system.

The paper is organized into six sections. Section 2 outlines the procedure for designing an aerocapture maneuver; in the Section 3 details of the FSI technique are provided; Section 4 provides details on the HIAD geometry used for testing and about the structural model used in this work; Section 5 introduces the process of generating the aerodynamic database, a static stability analysis of the proposed capsule and a control system simulations in the presence of random density perturbations; an example of an inflation system is presented in Section 6.

2. Nominal and non-Nominal aerocapture maneuvers

In this study, we analyze the aerocapture maneuver of a SmallSat approaching Mars.

The trajectory is computed using the following 3-degrees-of-freedom system of ODEs, see [22]:

$$\frac{dU_\infty}{dt} = g\sin\gamma - \frac{1}{2}\rho_\infty(z)U_\infty^2\frac{1}{\beta} \tag{2a}$$

$$\frac{d\gamma}{dt} = \frac{g\cos\gamma}{U_\infty} - \frac{U_\infty}{R_p + z}\cos\gamma \tag{2b}$$

$$\frac{dz}{dt} = -U_\infty\sin\gamma \tag{2c}$$

where $g = 3.71\ \mathrm{m/s^2}$ is the Martian gravitational acceleration, $R_p = 3389.5$ km is the planet's radius, γ is the re-entry flight-path angle, and $\beta = m/C_D A$ is the ballistic coefficient defined as the ratio between the mass m of the spacecraft and the drag area $C_D A$. The initial conditions for the system (2) are based on typical SmallSat Mars reentry data [2]: an initial velocity of 6 km/s, an initial reentry angle of 8.52°, and an initial atmospheric entry altitude of 120 km. The vertical profile of atmospheric density $\rho_\infty(z)$ is obtained from the Mars Climate Database [23,24].

Fig. 1 compares two aerocapture trajectories with different ballistic coefficients. A ballistic coefficient of $\beta = 60\ \mathrm{kg/m^2}$ corresponds to the Pathfinder capsule with a rigid heat shield, while $\beta = 20\ \mathrm{kg/m^2}$, represents a spacecraft equipped with an inflatable heat shield, which provides three times the cross-sectional area of the Pathfinder's rigid shield. As shown in Fig. 1a, for the same initial reentry angle γ_0, the rigid heat shield (blue line) results in a significantly higher exit velocity. In contrast, Fig. 1b demonstrates that achieving the same exit velocity with a rigid heat shield requires braking at lower altitudes, where mechanical and thermal loads are considerably greater.

Fig. 2 depicts the nominal aerocapture trajectory of a spacecraft equipped with an inflatable heat shield. The spacecraft has a mass of 61 kg and a cross-sectional area of 1.767 $\mathrm{m^2}$ [2], yielding a ballistic coefficient of $\beta = 26.6\ \mathrm{kg/m^2}$. The plot shows that the spacecraft enters the Martian atmosphere at a Mach number exceeding 28 and exits at approximately $M_\infty = 17$. The primary deceleration occurs at an altitude of around 60 km above the planet's surface.

As discussed in Sect. 1, small variations in atmospheric density can have a significant impact on the success of aerocapture maneuvers. Fig. 3 compares the nominal trajectory with those resulting from a ±5% deviation in atmospheric density. An increase of +5% (red curve) causes the spacecraft to descend too rapidly, leading to mission failure due to planetary impact. In contrast, a −5% decrease in density (blue solid line) results in a higher atmospheric exit velocity. Although this velocity remains below Mars' escape threshold, the spacecraft enters a stable, but higher orbit.

The Mars-GRAM model [8] indicates that atmospheric density at aerocapture altitudes can fluctuate by 10% to 20% from the nominal mean value. Additionally, anomalies in solar activity and dust storms can induce even greater density variations [25], significantly impacting the aerocapture process. These uncertainties underscore the necessity of compensatory techniques to mitigate the effects of atmospheric variability. To this end HIADs, designed to decelerate the spacecraft, can continuously adapt to the unexpected atmospheric density variations encountered during flight. The proposed continuous drag modulation technique leverages the HIAD's ability to adjust its cross-sectional area-and, consequently, its ballistic coefficient-by controlling the pressure difference between its internal inflation and the external aerodynamic pressure loading. In addition to modifying the cross-sectional area, changes in inflation pressure also influence the aerodynamic drag coefficient, which depends upon the shield's shape. By dynamically adjusting the inflation pressure, the technique continuously regulates the $C_D A$ product throughout atmospheric entry, ensuring that $\rho_\infty C_D A$-and thus the drag-remains as close as possible to its nominal value.

2.1. Drag modulation control system

The continuous drag modulation technique proposed in this study requires a control system capable of adjusting the shield's shape based

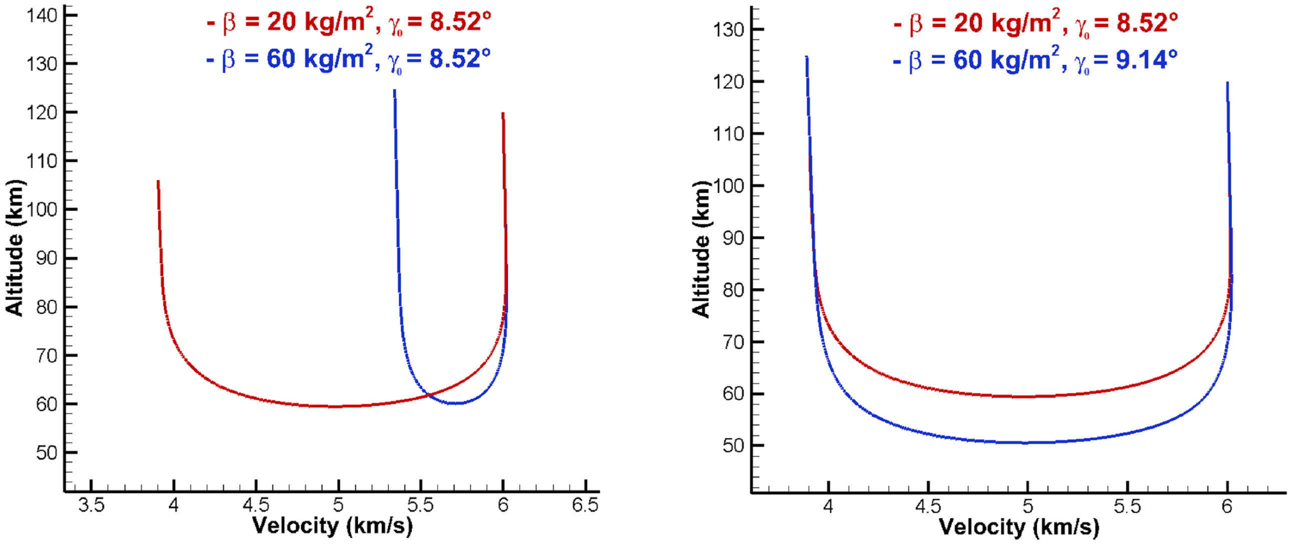

a)   b)

Fig. 1. a) Comparison of two trajectories with different β values and the same γ_0; b) Comparison of two trajectories with different β values and the same exit velocity from the atmosphere.

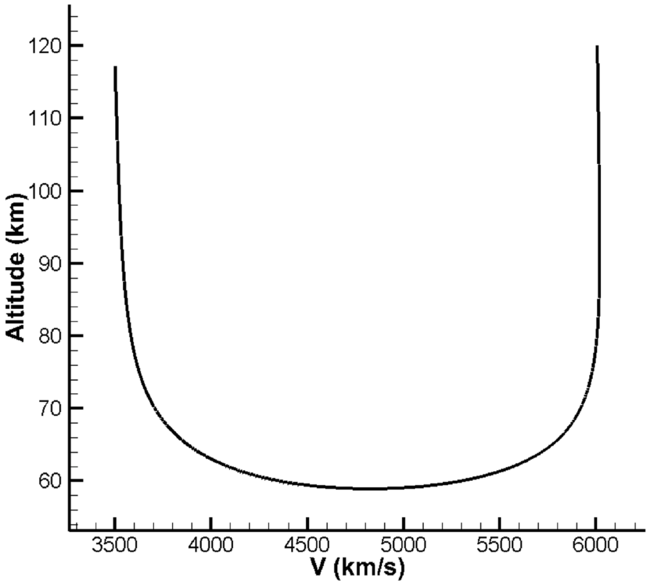

Fig. 2. Nominal aerocapture trajectory.

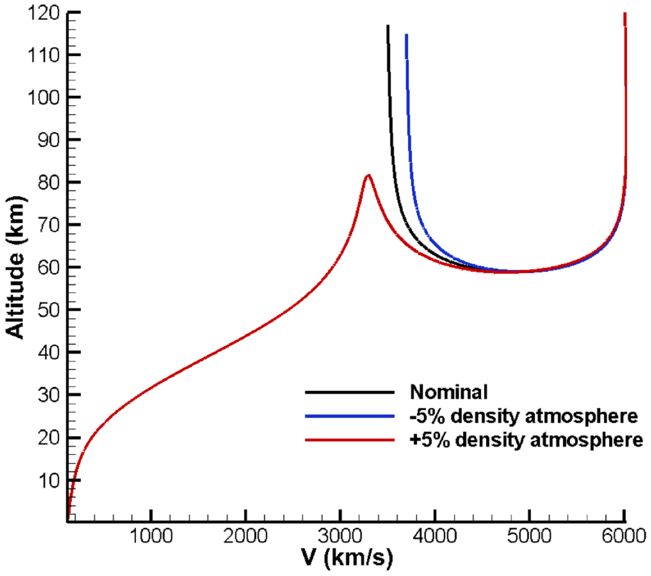

Fig. 3. Nominal trajectory vs. perturbed trajectories with ±5% atmospheric density variation.

on external atmospheric density conditions. This system, sketched in Fig. 4, relies on an accelerometer to measure the actual spacecraft's acceleration, a^n, during atmospheric flight and compare it with its nominal value, a^0. Additionally, two pressure sensors measure the differential pressure (Δp_{inf}) between the internal inflation pressure and the external stagnation pressure at the rigid nose of the shield.

The control system operates as follows:

- Initial Configuration: The spacecraft begins the aerocapture maneuver outside the atmosphere with the HIAD in its nominal configuration, set at the nominal differential pressure, $(\Delta p_{\text{inf}})^0$, corresponding to the nominal $(C_D A)^0$ value.
- **Acceleration Monitoring:** The onboard accelerometer measures the current acceleration (a^n) and detects deviations from the nominal value by evaluating the ratio a^n/a^0. If $a^n/a^0 \neq 1$, the control system computes a new required drag area:

$$(C_D A)^n = \frac{a^0}{a^n}(C_D A)^0.$$

- Pressure Adjustment: The system selects a new differential pressure $(\Delta p_{\text{inf}})^n$ that produces the required $(C_D A)^n$.
- Shield Inflation/Deflation: the system inflates or deflates the shield until the differential pressure reaches $(\Delta p_{\text{inf}})^n$, ensuring the desired aerodynamic response.

This control sequence is repeated throughout the atmospheric passage to correct for any further unexpected density variations.

To enable this control process, a precise correlation between Δp_{inf} and $C_D A$ is required. This relationship is established by constructing an aerodynamic database using multiple FSI simulations at various points

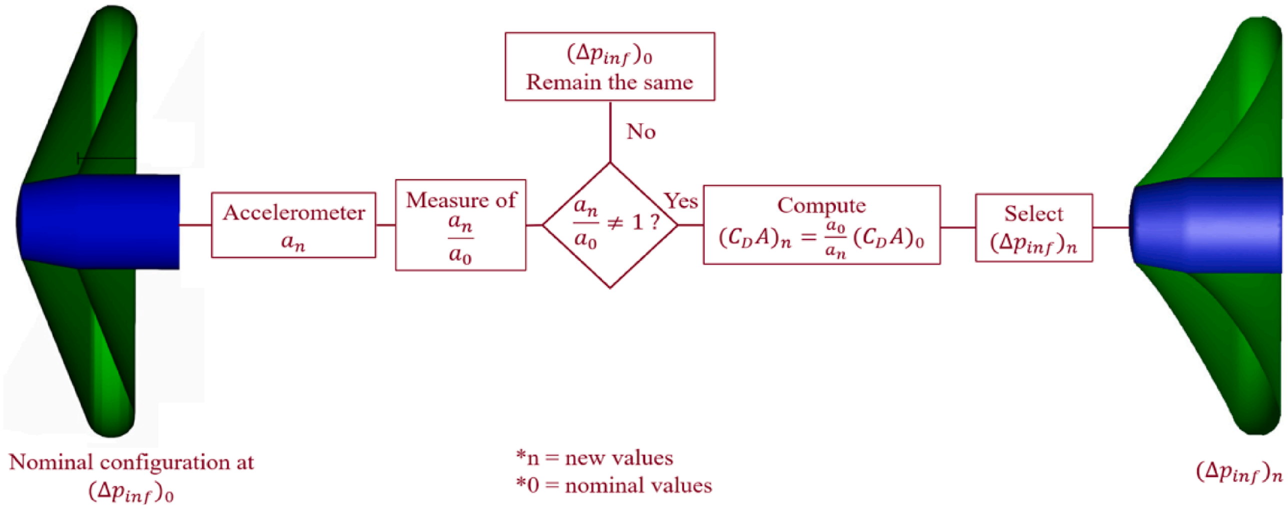

Fig. 4. Conceptual diagram of the control system operation.

along the nominal trajectory. These simulations characterize how $C_D A$ varies with Δp_{inf} under different flight conditions.

3. Fluid-Structure interaction technique

To determine the correct values of $C_D A$ associated with a given Δp_{inf} along the spacecraft's atmospheric trajectory, the steady-state FSI technique developed and validated by Orlandini et al. [6,16,17] was employed to compute the equilibrium configuration of inflatable structures in hypersonic flow.

This approach applies the front-tracking methods to model both the bow shock ahead of the HIAD and the thin membrane comprising the deformable shield. These elements are represented as double-sided surfaces with negligible thickness, whose motion is governed by the appropriate equations: the Rankine-Hugoniot jump conditions for the gasdynamic discontinuity and a nonlinear elastic membrane model [26] for the inflatable section of the HIAD. A key advantage of front-tracking [27] (also known as shock-fitting [28] when applied to gas-dynamic discontinuities) in modeling the bow shock is its low numerical error, enabling the use of coarser meshes compared to traditional shock-capturing approaches.

The FSI algorithm is loosely coupled in the sense that the fluid and structural solvers are executed sequentially: the gasdynamic solver provides the pressure distribution on the outer surface of the shield, while the structural solver computes the updated shape under the combined action of the aerodynamic and inflation pressures.

The computational procedure can be summarized as follows.

Step 1: Mesh generation. A background tetrahedral grid is created to fill the domain surrounding both the bow shock and the inflatable structure. The surface meshes of these interfaces are inserted into the background grid, and all intersected elements are removed to form cavities that are then locally remeshed using the Delaunay-based `tetgen` [29] generator. The resulting *computational mesh* conforms to both discontinuity surfaces and excludes the region inside the HIAD, where a constant inflation pressure is assumed.

Step 2: CFD solution. The gasdynamic solution is computed using the `UnDiFi-3D` shock-fitting module [19,30], while the HIAD shape is held fixed. The shock motion is governed by the Rankine-Hugoniot jump relations, whose solution provides the shock speed, w, used to update the shock position.

At each iteration, the `eulfs` [31,32] solver, which implements a second-order accurate *Residual Distribution (RD)* scheme, computes the solution of the Euler equations in the smooth regions bounded by the moving discontinuity surfaces. Convergence is achieved when w asymptotically vanishes, indicating that both the shock geometry and the flow field have reached a steady configuration, while the HIAD geometry remains fixed during this step.

Step 3: Structural deformation. The deformation of the inflatable shield is computed using a nonlinear finite-element model implemented inside MSC-Nastran [33].

The nonlinear system is solved, at each iteration i, assembling the tangent stiffness matrix $\mathbf{K}_T^{(i)} = \mathbf{K}_m + \mathbf{K}_d$ as the sum of the material stiffness, $\mathbf{K}_m$ and differential stiffness, $\mathbf{K}_d$ caused by the initial stress, and the displacement increment $\Delta\mathbf{d}$ is obtained from:

$$\mathbf{K}_T^{(i)} \Delta\mathbf{d} = \mathbf{R}^{(i)} \tag{3}$$

where $\mathbf{R}$ is the residual vector.

The input loads consist of a constant uniform inflation pressure, p_{inf}, applied on the inner surface of the HIAD and a spatially varying aerodynamic pressure distribution computed by the `eulfs` solver on the outer surface.

Since the analysis is limited to steady conditions, the inertial effects of the HIAD are neglected in the structural simulation. Consequently, the resulting deformation depends solely on the differential pressure acting on the two sides of the membrane and on its elastic properties.

This assumption simplifies the structural problem because the inflation and deflation behavior of the HIAD is evaluated as a sequence of quasi-static equilibrium configurations.

Step 4: Geometry update. After the structural computation, the HIAD surface is displaced, altering the computational domain. A local remeshing procedure is then performed to regenerate the computational grid around the updated geometry.

The four steps are repeated until both the aerodynamic pressure field and the structural deformation converge to steady values, see [17] for more details.

The present FSI technique relies on an inviscid (Euler) flow solver, which neglects viscous effects and, consequently, the contribution of skin friction to the total aerodynamic load. However, this assumption does not compromise the accuracy of the computed drag for hypersonic blunt bodies. Numerical and experimental studies [34] have shown that, at hypersonic speeds, the pressure contribution dominates the total aerodynamic force for more than 98% of the total drag, while the skin-friction component is two to three orders of magnitude smaller. Therefore, the pressure field predicted by the Euler solver accurately represents the physical load driving the deformation of the inflatable shield.

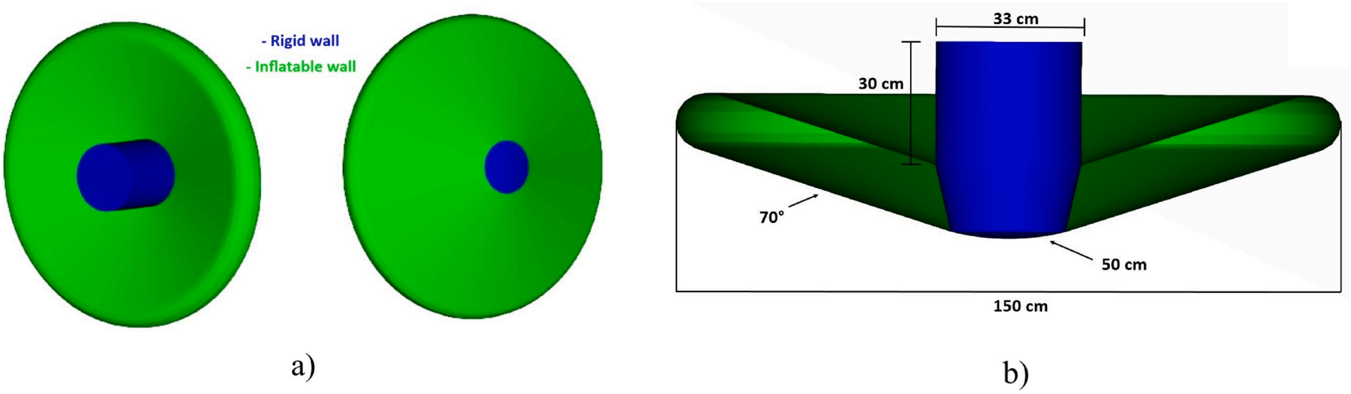

Fig. 5. a) HIAD front-view and back-view; b) Nominal HIAD geometry.

Conversely, the assumption of steady-state equilibrium introduces a more significant modeling limitation. However, since the characteristic timescale of the structural deformation of the HIAD is orders of magnitude larger than the aerodynamic flow-adjustment timescale, the assumption that flow field instantaneously adapts to the structural deformation is reasonable. Therefore, the present steady-state framework effectively captures the quasi-static aerodynamic response of the HIAD. Future work will nonetheless focus on extending the formulation to assess dynamic stability and transient aeroelastic effects through a fully coupled unsteady aeroelastic-aerothermodynamic model of the inflatable shield.

4. Design of hypersonic inflatable aerodynamic decelerators

The nominal SmallSat shape is based on the design by Deshmukh et al. [2], shown in Fig. 5.a and has the dimensions reported in Fig. 5.b. The shield consists of an inflatable section (green) and rigid components (blue), including a rigid nose with a 50 cm radius and a rear section that represents the satellite. The shield has a diameter of 1.5 m and a cone angle of 70°.

The inflatable shield's structural and thermal-protection systems meet demanding requirements: they are highly lightweight and compactly stowed, yet once deployed withstand extreme aerodynamic loads, high heat fluxes and large deformations during atmospheric entry. For this reasons HIADs are made of F-TPS capable of withstanding surface heat fluxes up to approximately 80 $\mathrm{W/cm^2}$, as demonstrated in recent missions such as LOFTID [35].

To quantify the heat flux during the passage in the Martian atmosphere, the Sutton-Graves formula [36] was used

$$\dot{q}_c = k_m \sqrt{\frac{\rho_\infty}{R_N}} U_\infty^3 \tag{4}$$

where R_N represents the radius of the heat shield nose and k_m is a constant that depends on the Martian atmosphere whose value in SI unit is 1.83×10^4. Fig. 6 illustrates the convective heating rate at the stagnation point, as determined using Eq. (4). The curve reaches a peak value of 25 W/cm^2 at the nose, where the shield is rigid, so the heat flux along the inflatable shield will be reasonably lower than this value. In any case the maximum value of the heat flux shown in Fig. 6 falls within the thermal tolerance of F-TPS and, in general, of the materials commonly used in inflatable structures [2].

4.1. Structural model description

The inflatable heat shield is modeled as a thin flexible membrane made of 1 mm thick Kapton fabric [37], with Young's modulus $E = 2.6$ GPa, Poisson's ratio $\nu = 0.33$, and density $\rho = 1420\ \mathrm{kg/m^3}$. The structural response of the membrane is computed using the nonlinear static solver `SOL400` in MSC Nastran [21], following the methodology outlined in the Step 2 of Section 3. The central rigid part (in blue) is fully constrained, *i.e.*, all translational and rotational degrees of freedom (D.O.F.) are fixed. The inflatable annular region (in green) is instead modeled as a deformable membrane. To reproduce membrane-like behavior and avoid spurious bending stiffness, the rotational D.O.F. of the inflatable region are constrained, while the translational D.O.F. are left free to respond to the applied loads. The mesh consists primarily of CQUAD4 shell (membrane) elements, supplemented by CTRIA3 elements of the rigid part. In the representative mesh reported in Fig. 7, the model includes 1925 nodes, 1200 CQUAD4 elements and 1246 CTRIA3 elements.

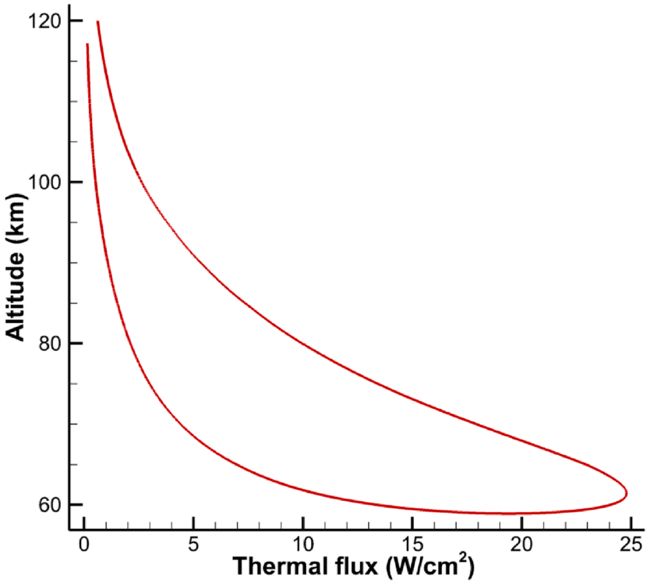

Fig. 6. Thermal flux in the stagnation point during the aerocapture maneuver.

5. Numerical analysis

5.1. FSI Model and computational mesh

The FSI simulations were performed using the front-tracking approach described in Section 3. The computational model, with the boundary conditions used in the simulations, is shown in Fig. 8. The domain extends 9.5 m in both the streamwise (X) and vertical (Y) directions and 7.5 m in the spanwise (Z) direction.

The background tetrahedral mesh fills the entire domain except for the regions occupied by the HIAD and the bow shock, which are treated as internal boundaries. Both surfaces are inserted into the background

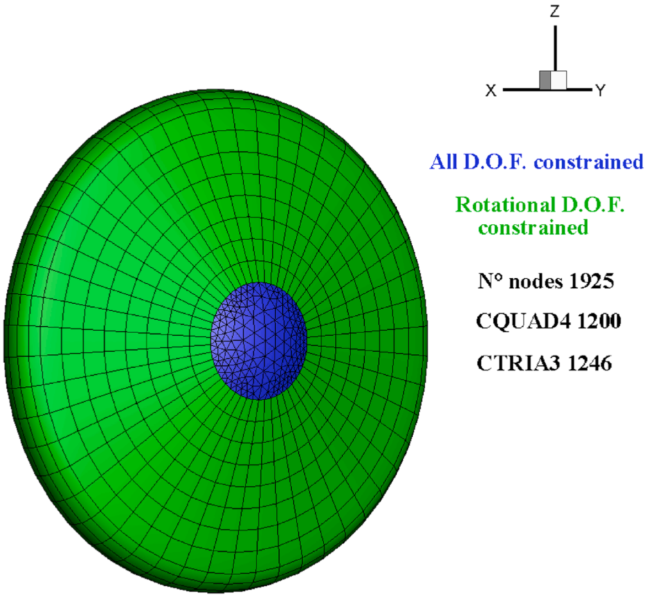

Fig. 7. Structural mesh of the HIAD. The rigid part (blue) is fully constrained. The inflatable membrane (green) is modeled with predominantly CQUAD4 elements; only the rotational D.O.F. are constrained in this region to enforce membrane kinematics. (For interpretation of the references to colour in this figure legend, the reader is referred to the web version of this article.)

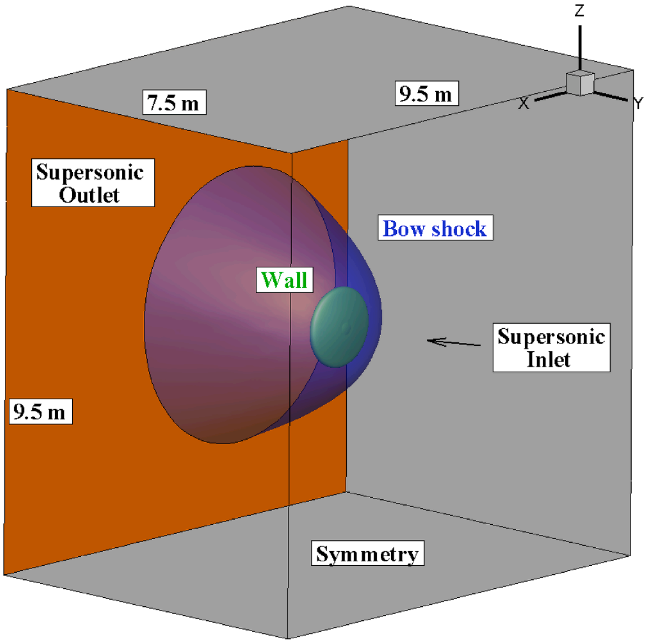

Fig. 8. Computational domain and boundary conditions used in the FSI model. The bow shock and wall surfaces are explicitly fitted, while the supersonic inlet/outlet and symmetry plane define the external boundaries.

Table 1
Mesh characteristics for the CFD model.

Region	Nodes	Elements	Element type
Background grid	22,184	108,328	Tetrahedra
HIAD surface	3080	6156	Triangles
Shock surface	5506	10,866	Triangles

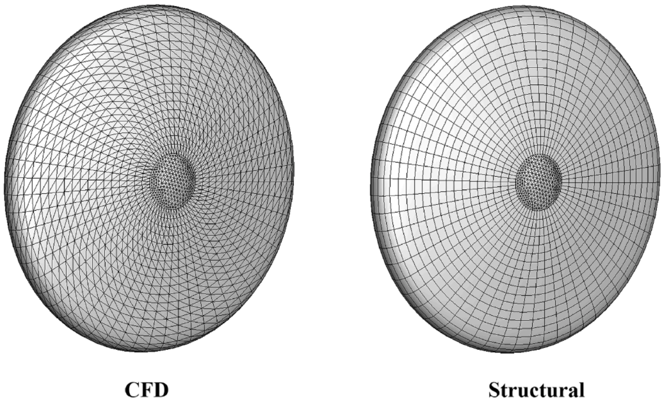

Fig. 9. Comparison between the CFD (left) and structural (right) surface meshes. The CFD model employs triangular elements for compatibility with the `eulfs` solver, while the structural model uses quadrilateral CQUAD4 elements for improved membrane accuracy.

Table 2
Mesh characteristics of the structural model.

Region	Nodes	Elements	Element type
Membrane	2460	2400	CQUAD4
Rigid parts	620	1356	CTRIA3

grid using the Delaunay-based `tetgen` [29] mesh generator. Cells intersecting these surfaces are removed and locally remeshing, ensuring conformity between the computational mesh and the discontinuity surfaces. As summarized in Table 1, the background grid includes approximately 1.1×10^5 tetrahedral elements and over 2.2×10^4 nodes, while the HIAD and bow-shock surfaces are discretized using 6,156 and 10,866 triangular elements, respectively.

Fig. 9 compares the surface meshes used in the CFD and structural solvers. The CFD mesh (left) employs a triangular discretization consistent with the `eulfs` solver, which uses tetrahedral control volumes and requires surface triangulations.

Conversely, the structural mesh (right) is composed primarily of CQUAD4 shell elements to accurately capture membrane behavior. Indeed, according to the MSC software user guide [21], quadrilateral elements are less stiff and more accurate than their triangular counterpart, particularly for modeling membrane strain. Therefore, to maintain the same geometric position of the grid points and to avoid interpolation when the pressure distribution calculated by the CFD code is transferred to the structural solver, each quadrilateral cell is divided into two triangular elements. The rigid parts, that do not deform, are also disctretized with CTRIA3 elements.

In the structural model, see Section 4.1, all degrees of freedom of the rigid parts are constrained, while the inflatable part is free to deform under the applied loads. Rotational degrees of freedom on the membrane are fixed to prevent artificial bending stiffness, ensuring pure membrane response. The corresponding structural mesh characteristics are listed in Table 2. The model includes 3080 nodes like the CFD mesh with 2400 CQUAD4 membrane elements, and 1356 CTRIA3 elements related to the rigid parts.

5.2. *FSI Results*

For the sake of simplicity, in this paper, the database was build considering five points along the aerocapture nominal trajectory with the corresponding freestream conditions (M_∞, U_∞, z, ρ_∞, p_∞), reported in Table 3 and six distinct differential inflation pressures (4 kPa, 8 kPa, 11kPa, 12 kPa, 16 kPa and 20 kPa) for a cumulative total of 30 simulations.

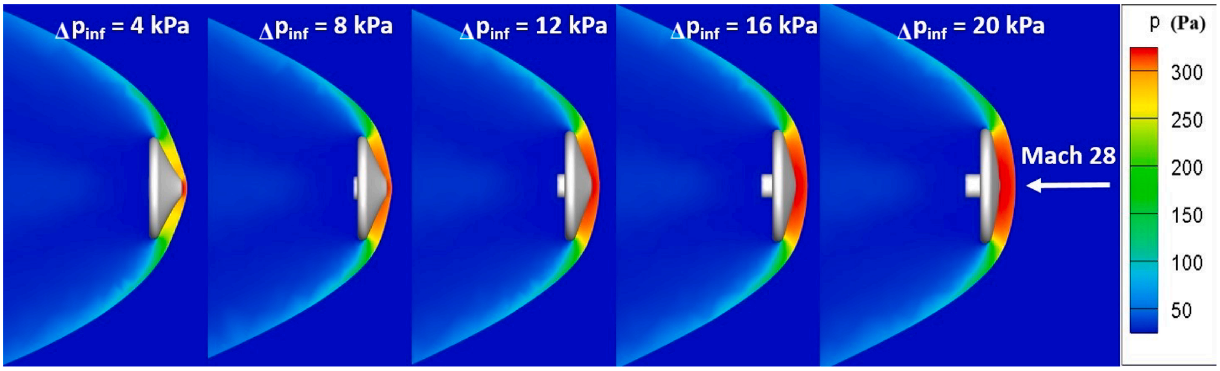

Fig. 10. FSI pressure fields in the YZ plane at $M_\infty = 28$ corresponding to different Δp_{inf} values.

Table 3
Altitude and corresponding free-stream conditions along the aerocapture trajectory.

M_∞	z (km)	U_∞ (m/s)	ρ_∞ (kg/m^3)	p_∞ (Pa)
28	68.61	5880	1.27E-05	0.35
26	61.06	5460	3.21E-05	0.92
24	59.13	5040	4.07E-05	1.17
22	59.08	4620	4.09E-05	1.18
20	60.90	4200	3.27E-05	0.93

Fig. 10 shows the pressure fields in the YZ plane at $M_\infty = 28$ for the five values of Δp_{inf}. Variations in Δp_{inf} modify the shield geometry, leading to changes in both the drag coefficient and the cross-sectional area. Consequently, the product $C_D A$ is a function of Δp_{inf}.

The aerodynamic database, shown in Fig. 11 by plotting $C_D A$ versus M_∞, is obtained from Eq. (1) in which the aerodynamic drag was calculated by integrating the pressure obtained from the FSI simulations.

Each curve corresponds to a specific differential pressure condition, with the nominal case at $\Delta p_{\text{inf}} = 11\,\text{kPa}$ represented by the black curve with “x” markers in Fig. 11, yielding $C_D A = 2.35\,\text{m}^2$. The choice of $\Delta p_{\text{inf}} = 11 kPa$ as nominal value appears natural when looking at Fig. 11. Comparing this nominal value with the case $\Delta p_{\text{inf}} = 4\,\text{kPa}$ (gray curve with square markers) shows a reduction of more than 20% in $C_D A$. Thus, decreasing the inflation pressure from 11 kPa to 4 kPa enables compensation for an atmospheric density increase of up to +20%, consistent with the maximum deviation of the mean density in the Martian atmosphere at typical aerocapture altitudes. Conversely, increasing Δp_{inf} from 11 kPa to 20 kPa raises $C_D A$ by 23.4%, allowing compensation for a density reduction of about -20%. Overall, the proposed shield can offset density variations from +20% to -23.4% by adjusting Δp_{inf} between 4 and 20 kPa.

This choice ensures robustness of the aerocapture maneuver, since the inflatable shield is able to compensate for density variations of ±20 that are typical (according to the Mars-GRAM model) of the altitudes at which the aerocapture maneuver takes place. In addition to mean density variations, transient phenomena such as Martian dust storms can further perturb the atmosphere. Whiters and Pratt [25] showed that typical dust storms can increase upper-atmosphere density by more than 100%, particularly near the poles. Even under such conditions, the probe retains sufficient capability to avoid catastrophic outcomes, such as impact with the surface or escape from orbit. If the density increase becomes excessive, the shield could be jettisoned, thus reducing the cross-sectional area to the rigid nose shown in Fig. 5; in this configuration, the HIAD geometry analyzed here can accommodate density increases of up to 94%. Conversely, an excessive density reduction could allow the spacecraft to exit the atmosphere with a velocity exceeding escape speed, but this occurs only for reductions greater than 55% relative to the nominal case. Although the proposed drag modulation technique compensates only up to a 23.4% density decrease, the aerocapture maneuver remains feasible, since capture would fail only if the reduction exceeded 55%.

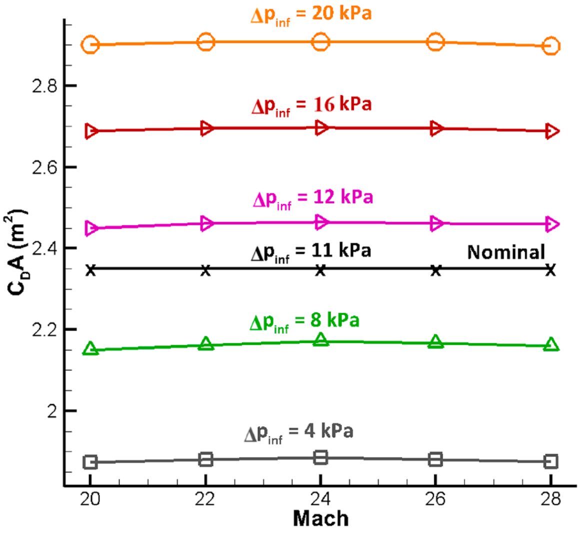

Fig. 11. Aerodynamic database.

5.3. Stability analysis of the HIAD

Further CFD analyses were performed to verify the longitudinal static stability of the capsule analyzed in the present work. To investigate static stability, the FSI technique described in Section 3 was applied to compute the aerodynamic pitch moment coefficient, C_m, at different freestream condition along the trajectory and different angles of attack (AoA). For instance, Fig. 12 shows the numerically computed flow-field at $M_\infty = 24$ and $\Delta p_{\text{inf}} = 20\,\text{kPa}$ when the AoA ranges between 0° and 20° in steps of 5°.

These numerical solutions were used to calculate the pitching moment coefficient with respect to the gravity center which, for the present geometry, is located on the symmetry axis at 43.21% of the distance between the nose and the rear part of the capsule. The static stability analysis is based on the general aerodynamic formulation by Hirschel and Weiland [38], in which the aerodynamic moments about an arbitrary reference point are related to the aerodynamic force coefficients. When the reference point coincides with the center of gravity (cog), the trim condition requires that

$$C_{m|cog} = 0. \tag{5}$$

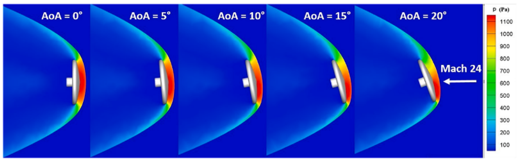

Fig. 12. FSI pressure field at $M_\infty = 24$ in the YZ plane for different angles of attack.

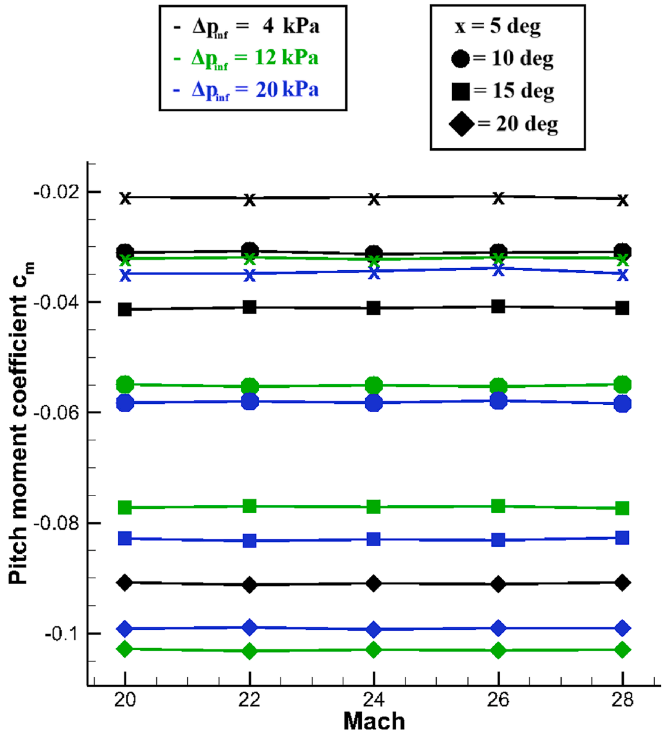

Fig. 13. Pitch moment coefficient w.r.t. M_∞.

and the longitudinal static stability is guaranteed if the sign of its derivative with respect to the angle of attack is

$$\frac{\partial C_{m|cog}}{\partial \alpha} < 0, \tag{6}$$

Fig. 13, where C_m is plotted against M_∞ at four different values of the AoA and three different values of Δp_{inf}, clearly reveals that the hypersonic Mach number independence principle is sufficiently well verified, since the pitching moment coefficient remains nearly constant as the Mach number varies.

This observation enables the analysis of capsule stability at a representative point along the aerocapture trajectory, with results extendable to other trajectory points. The aerodynamic pitching moment coefficient was evaluated using numerical simulations with varying AOA and three different Δp_{inf} values equal to 4, 12, and 20 kPa, under a fixed flight condition of $M_\infty = 24$. The results, shown in Fig. 14, confirm the capsule's static stability: both the pitching moment coefficient and its derivative w.r.t. the AoA remain negative for all values of Δp_{inf}.
The aerodynamic characteristics of an HIAD are expected to be weakly sensitive to small variations in the AoA. Indeed, flight data obtained from the LOFTID [39] mission show perturbations of the angle of attack typically below 1° around the trim condition. Our numerical estimates indicate that a variation of 1° in the angle of attack at $M_\infty = 24$ produces a change of $C_D A$ less than 0.3% compared to the zero-angle configuration. This suggest that moderate attitude oscillations have a negligible impact on the overall aerodynamic performance and on the modulation of the drag force.

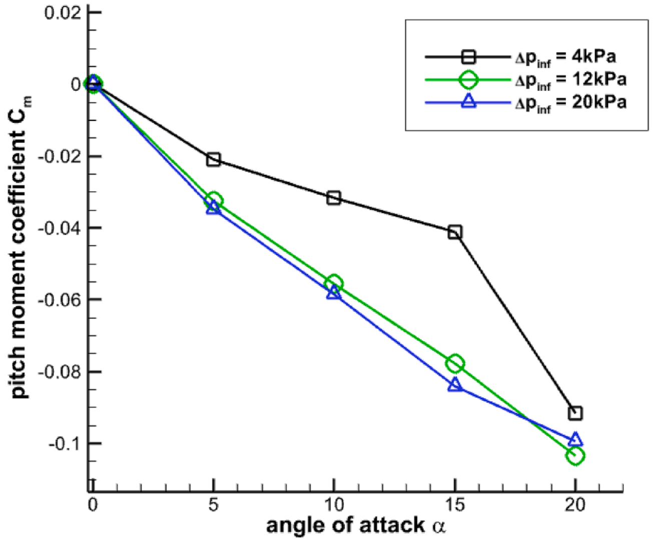

Fig. 14. Pitch moment coefficient w.r.t. the AoA for three different inflation pressures.

5.4. Control system analysis

This section presents the performance analysis of the proposed continuous drag modulation control system when random atmospheric density perturbations between +20% and +50% are introduced along the nominal aerocapture trajectory, as shown in Fig. 15.
The control system follows the architecture discussed in Section 2.1, The measured acceleration is compared with its nominal value and, then, the HIAD inflation pressure is adjusted using the aerodynamic database linking Δp_{inf} to $(C_D A)$.
The control loop is not active for the entire flight, but only during the portion of the trajectory where the vehicle experiences significant aerodynamic loads and density variations. As shown in Fig. 16, the control system is enabled when the spacecraft enters the dense region of the Martian atmosphere (around 75 s after atmospheric entry) and deactivated after approximately 260 s, once the vehicle exits the high-drag portion of the trajectory. During this interval, the modulation system adjusts the inflation pressure to maintain the nominal drag level despite the fluctuating external density.

As shown in Fig. 17, where the nominal trajectory is shown using a solid black line, in the absence of drag modulation, random density fluctuations (up to 50% above nominal) increase aerodynamic drag, causing stronger deceleration and an earlier descent (red line) that ends in surface impact.

To counteract the detrimental effect of the unexpected density perturbations, the drag modulation system is activated. The influence of the HIAD dynamics on control performance is evaluated assuming three different characteristic response times, T_{resp}, each representing the time required for the effective drag area $(C_D A)$ to vary between its minimum and maximum configuration (corresponding to a differential pressure change between 4 and 20 kPa). The average variation rates $\left(\left.\frac{\partial(C_D A)}{\partial t}\right|_{av}\right)$ are summarized in Table 4.

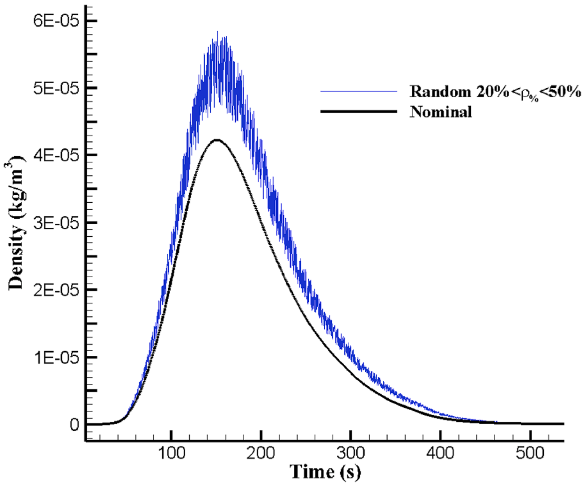

Fig. 15. Random density perturbation between +20% and +50% relative to nominal.

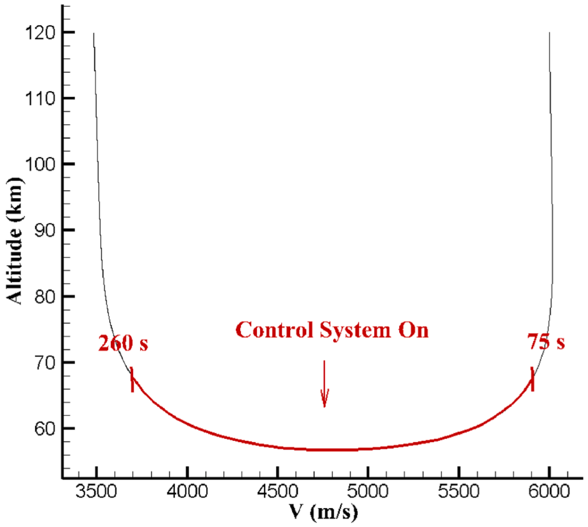

Fig. 16. Nominal trajectory showing the activation window of the control system.

Table 4
HIAD response times and ($\left.\frac{\partial(C_DA)}{\partial t}\right|_{av}$) variation rates.

T_{resp}	$\left.\frac{\partial(C_DA)}{\partial t}\right\|_{av}$
10 s	0.107 (m^2/s)
60 s	0.0178 (m^2/s)
120 s	0.0089 (m^2/s)

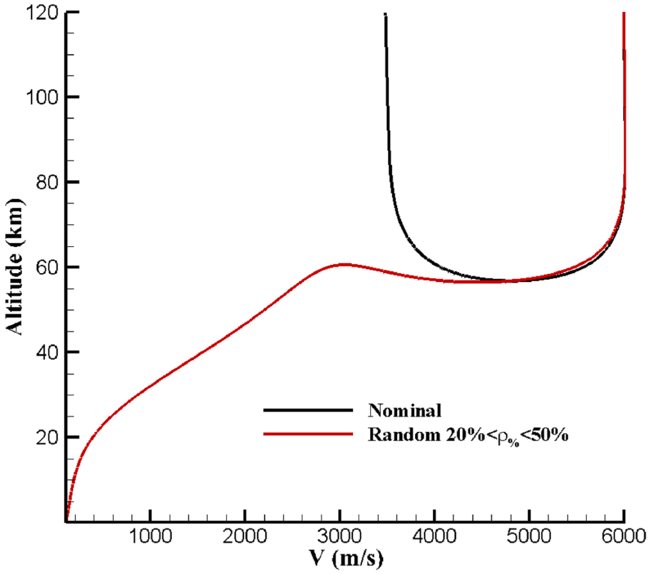

Fig. 17. Effect of a random 20-50% density increase without drag modulation.

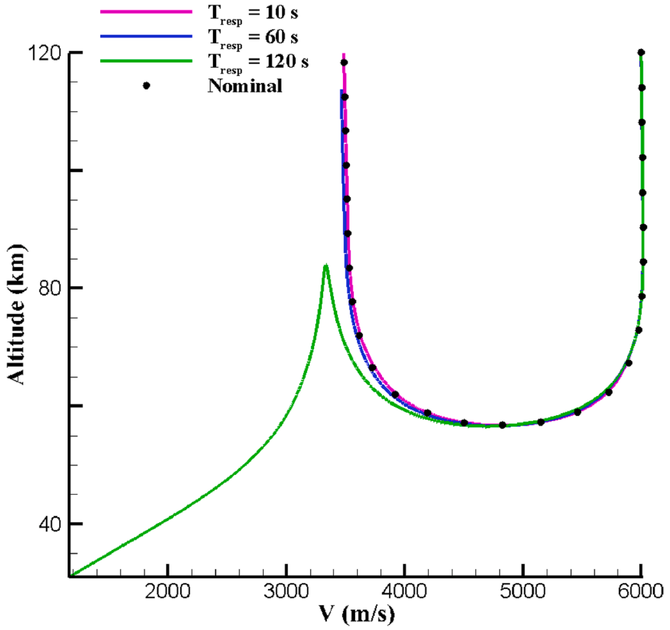

Fig. 18. Controlled trajectories for different HIAD response times.

Shorter response times are expected to enable faster drag modulation, thereby improving the system's ability to counteract density disturbances. Results from three simulations, each characterized by a different response time, show that the effectiveness of inflation pressure modulation in compensating random density disturbances depends on the response time. The corresponding trajectories for the three assumed HIAD response times are compared in Fig. 18. The case with $T_{\text{resp}} = 10$ s (magenta line) nearly overlaps the nominal trajectory (black dots), indicating that the control system can fully compensate for the density anomalies. For $T_{\text{resp}} = 60$ s (blue), the system still maintains capture conditions, although with a slightly lower exit velocity. When $T_{\text{resp}} = 120$ s, the shield's slow reaction prevents effective compensation, resulting in excessive deceleration and impact with the surface. It should be noted that a linear time variation of C_DA is assumed and that the aerocapture maneuver has a total duration of the order of 5 minutes. Within this time frame, response times of one minute already represent relatively slow actuation compared to the maneuver timescale. The present results therefore indicate that response times significantly shorter than the maneuver duration, of the order of 60 s or less, are sufficient to ensure robust aerocapture under 50% density fluctuations.

Figs. 19 and 20 display the time evolution of the controlled variables for the three response times. Fig. 19 shows the variation of the effective drag area (C_DA), while Fig. 20 reports the corresponding differential inflation pressure computed from the aerodynamic database. For the fastest response ($T_{\text{resp}} = 10$ s), C_DA rapidly adapts to the target value and follows high-frequency density fluctuations. As T_{resp} increases, both C_DA and Δp_{inf} vary more slowly, introducing a lag in drag compensation that leads to cumulative trajectory deviation. The relationship between

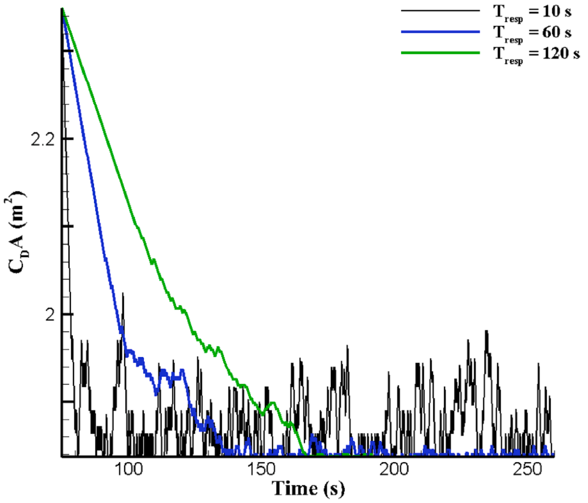

Fig. 19. Time evolution of C_DA for different T_{resp}.

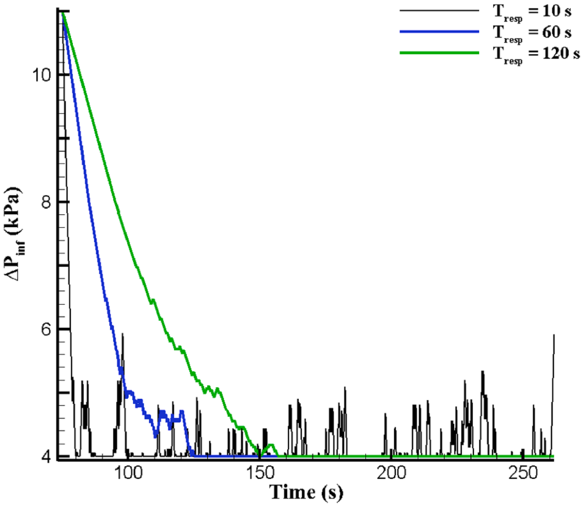

Fig. 20. Corresponding variation of Δp_{inf} obtained from the aerodynamic database.

the C_DA and Δp_{inf} curves confirms the reliability of the aerodynamic database used by the control algorithm.

6. Inflation system

One of the critical aspect in the design of the present continuous drag modulation technique is the inflation system. The recent test of the LOFTID inflatable shield [40], which has flown in November 2022, used an inflation system based on pressurized gas cylinders and pyrotechnic valves. Nevertheless, these devices cannot be employed for aerocapture missions towards distant planets or moons because of the following two main reasons:

1. it is difficult to ensure that a gas cylinder keeps the gas pressurized for a long time;
2. the pyrotechnic valves are single-use, whereas in our case, valves capable of multiple openings and closings are required.

To overcome the aforementioned problems, Cool Gas Generators (CGG), such as those described in [41], could be used instead. These devices are specifically designed for long term missions and have already been used in the Proba-2 mission [42] as a technology demonstration to validate the use of solid-state gas generators for propulsive applications. CGGs were also tested for membranes and are applicable not only to propulsion systems but also to inflatable structures [43]. CGGs consist in cartridges filled with solid propellant material that, once activated, undergoes a controlled chemical reaction to produce a cold inert gas (such as high-purity ($>99\%$) Nitrogen) that can be stored in a pressurized tank. The reaction completely consumes the propellant, ensuring maximum efficiency and leaving minimal residue. Subsequently, the gas generated by the CGG and stored in the tank can be transferred from a tank to the inflatable system using a network of valves and pipes.

The inflation system that can be envisaged for use in an aerocapture mission consists of a CGG-pressurized tank, a supply valve controlling gas flow to the inflatable shield, and an exhaust valve for reducing the inflation pressure. Prior to atmospheric entry, the CGG pressurizes the tank, and the stored gas inflates the heat shield to its nominal configuration. During atmospheric flight, the control system regulates the internal pressure to maintain the target differential pressure Δp_{inf} as commanded by the control system, either adding or releasing gas as needed. Consequently, the gas supply must be sufficient to achieve Δp_{inf} values above nominal, as required when atmospheric density is lower than expected and the product C_DA must be increased.

Based on these indications it is possible to estimate the mass of the inflation system. The amount of gas required for the aerocapture maneuver can be assessed by considering as reference values for the CGG the data reported in [41], where the gas output is 260 normal-l/kg for Nitrogen. To reach the nominal configuration the shield must be inflated at a differential pressure equal to 11 kPa. Since the shield's volume is 0.31 m^3, the required mass of Nitrogen equals 42.1 g, corresponding to 33.66 normal-liters. Since the CGG produces 260 normal-l/kg, the mass of the solid propellant should approximately equal 0.129 kg. This estimate considers the nominal mission but it does not take into account the mission drag modulation strategy. Considering the worst case scenario, to reach Δp_{inf} of 20 kPa the mass of the solid propellant increases to 0.235 kg. Finally, the mass of the inflation system, also including casings, tubes and valves, can be estimated, to equal 1% of the overall weight, in line with similar studies, see [44,45].

7. Conclusions

In this study, we presented a continuous drag-modulation system designed for the Mars orbit insertion of SmallSats. The approach seeks to maintain the nominal re-entry trajectory even when atmospheric density deviates from its expected value, causing variations in drag and consequently in vehicle velocity relative to the nominal design case. The proposed technique modifies both the drag coefficient and the cross-sectional area of an hypersonic inflatable aerodynamic decelerator to compensate for these density fluctuations, thereby keeping the aerodynamic drag as close as possible to its nominal value. In particular, C_DA is actively controlled by adjusting the inflation pressure within the shield. A feedback controller continuously acquires the measured acceleration from onboard accelerometers, compares it with the nominal reference and, using the calculated aerodynamic database that maps the differential inflation pressure to C_DA, modifies the HIAD pressure to correct the trajectory. For the analyzed shield, varying the inflation pressure over a range of approximately 15 kPa, is sufficient to offset mean density biases from approximately ± 20% at aerocapture altitudes on Mars. In the control system simulations with random density increases ranging between $+20\%$ to $+50\%$, the modulation effectively restores near-nominal flight when the time response of the shield is not larger than 60 seconds. These results demonstrate the effectiveness of the overall technique and that a relatively fast HIAD inflation response is essential to compensate for large density fluctuations.

The longitudinal static stability of the shield was also assessed numerically across several angles of attack, and the results confirmed that the capsule remains statically stable for all tested conditions.

Finally, a preliminary sizing of the inflation system indicates that a cold-gas generator is suitable for long-duration space missions, with the estimated mass of the system representing approximately 1% of the total spacecraft mass.

Future work will focus on expanding the aerodynamic database to improve the accuracy of the drag-modulation control, exploring alternative shield geometries to enlarge the compensation range for atmospheric density variations, and refining both the control system and inflation hardware, both of which are key elements for the successful implementation of the proposed technique.

CRediT authorship contribution statement

Valerio Orlandini: Writing – original draft, Software, Methodology, Data curation, Conceptualization; **Renato Paciorri:** Writing – review & editing, Supervision, Conceptualization; **Aldo Bonfiglioli:** Writing – review & editing, Supervision, Methodology, Conceptualization.

Data availability

No data was used for the research described in the article.

Declaration of interests

The authors declare that they have no financial, personal or other relationships with other people or organizations within three years of beginning the submitted work that could inappropriately influence, or be perceived to influence, their work.

Acknowledgment

The Ph.D. of Dr. Valerio Orlandini is funded by the European Union - Next Generation EU, Mission I.3.4 PNRR grants for digital and environmental transitions (Mission 4), Component 1, CUP B53C23001620006.

References

[1] B. Yost, S. Weston, G. Benavides, F. Krage, J. Hines, S. Mauro, S. Etchey, K. O'Neill, B. Braun, State-of-the-art small spacecraft technology (2021). https://ntrs.nasa.gov/api/citations/20210021263/downloads/2021_SOA_final_508_updated.pdf.

[2] R. Deshmukh, A. Bowes, S. Dutta, Small satellite aerocapture concepts for future interplanetary missions, in: AIAA SCITECH 2023 Forum, 2023, p. 0877. https://doi.org/10.2514/6.2023-0877

[3] A. Austin, A. Nelessen, B. Strauss, J. Ravich, M. Jesick, E. Venkatapathy, R. Beck, P. Wercinski, M. Aftosmis, M. Wilder, et al., Smallsat aerocapture to enable a new paradigm of planetary missions, in: 2019 IEEE Aerospace Conference, IEEE, 2019, pp. 1–20. https://doi.org/10.1109/AERO.2019.8742220

[4] V. Orlandini, R. Paciorri, A. Assonitis, A. Bonfiglioli, et al., Quantitative assessment of the mass-saving derived from mars aerocapture maneuvers, in: Proceedings of the 75Th International Astronautical Congress (IAC), 2024. https://iafastro.directory/iac/paper/id/85176/summary/.

[5] A.P. Girija, S.J. Saikia, J.M. Longuski, Y. Lu, J.A. Cutts, Quantitative assessment of aerocapture and applications to future solar system exploration, J. Spacecr. Rockets 59 (4) (2022) 1074–1095. https://doi.org/10.2514/1.A35214

[6] V. Orlandini, R. Paciorri, A. Assonitis, F. Saltari, A. Bonfiglioli, A fluid dynamics technique for modelling inflatable shield for re-entry or aerocapture missions, in: AIAA AVIATION 2023 Forum, 2023, p. 4425. https://doi.org/10.2514/6.2023-4425

[7] A. Duvall, C. Justus, V. Keller, Global reference atmospheric model (GRAM) series for aeroassist applications, in: 43Rd AIAA Aerospace Sciences Meeting and Exhibit, 2005, p. 1239. https://doi.org/10.2514/6.2005-1239

[8] H.L. Justh, Mars Global Reference Atmospheric Model 2010 Version: Users Guide, Technical Report, 2014. https://ntrs.nasa.gov/api/citations/20140003184/downloads/20140003184.pdf.

[9] H.L. Justh, J. Hoffman, Neptune Global Reference Atmospheric Model (Neptune-GRAM): User Guide, Technical Report, 2020. https://ntrs.nasa.gov/api/citations/20205001193/downloads/NASA_TM_20205001193.pdf.

[10] H.L. Justh, J. Hoffman, Titan Global Reference Atmospheric Model (Titan-GRAM): User Guide, Technical Report, 2020. https://ntrs.nasa.gov/api/citations/20205006805/downloads/NASA_TM_20205006805.pdf.

[11] M.K. Lockwood, K.T. Edquist, B.R. Starr, B.R. Hollis, G.A. Hrinda, R.W. Bailey, J.L. Hall, T.R. Spilker, M.A. Noca, N. O'Kongo, Aerocapture systems analysis for a Neptune Mission, Technical Report, 2006. https://ntrs.nasa.gov/api/citations/20060012088/downloads/20060012088.pdf.

[12] M.K. Lockwood, E.M. Queen, D.W. Way, R.W. Powell, K. Edquist, B.W. Starr, B.R. Hollis, E.V. Zoby, G.A. Hrinda, R.W. Bailey, Aerocapture systems analysis for a Titan mission, Technical Report, 2006. https://ntrs.nasa.gov/api/citations/20060007561/downloads/20060007561.pdf.

[13] D.N. Nguyen, S. Dutta, J. Green, H.K. Ali, Performance analysis of magnetohydrodynamic drag modulation for actively controlled aerocapture at neptune, in: 2024AAS/AIAA Astrodynamics Specialist Conference, AAS 24–382, 2024.

[14] Z.R. Putnam, R.D. Braun, Drag-modulation flight-control system options for planetary aerocapture, J. Spacecr. Rockets 51 (1) (2014) 139–150. https://doi.org/10.2514/1.A32589

[15] S. Hughes, J. Ware, J. Del Corso, R. Lugo, Deployable aeroshell flexible thermal protection system testing, in: 20Th AIAA Aerodynamic Decelerator Systems Technology Conference and Seminar, 2009, p. 2926. https://doi.org/10.2514/6.2009-2926

[16] V. Orlandini, R. Paciorri, A. Assonitis, F. Saltari, A. Bonfiglioli, A numerical technique for modelling hypersonic inflatable shields, in: XI International Conference on Textile Composites and Inflatable Structures, C. Lazaro, R. Rossi, R. Wuchne, 2023. https://doi.org/10.23967/c.membranes.2023.009

[17] V. Orlandini, R. Paciorri, A. Assonitis, A. Bonfiglioli, Front-Tracking Technique for Computing Inflatable Structures in Hypersonic Flows, AIAA J. 0 (0) 1–17. https://doi.org/10.2514/1.J065156

[18] R. Paciorri, A. Bonfiglioli, A shock-fitting technique for 2D unstructured grids, Comput. Fluids 38 (3) (2009) 715 – 726. https://doi.org/10.1016/j.compfluid.2008.07.007

[19] A. Bonfiglioli, M. Grottadaurea, R. Paciorri, F. Sabetta, An unstructured, three-dimensional, shock-fitting solver for hypersonic flows, Comput. Fluids 73 (2013) 162–174. https://doi.org/10.1016/j.compfluid.2012.12.022

[20] L. Campoli, A. Assonitis, M. Ciallella, R. Paciorri, A. Bonfiglioli, M. Ricchiuto, Undifi-2D: an unstructured discontinuity fitting code for 2D grids, Comput. Phys. Commun. 271 (2022). https://doi.org/10.1016/j.cpc.2021.108202

[21] Hexagon, MSC Nastran 2022.4 release guide (2022).

[22] J.D. Anderson, Hypersonic and high temperature gas dynamics, American Institute of Aeronautics and Astronautics, 2006. https://doi.org/10.2514/4.105142

[23] E. Millour, F. Forget, S.R. Lewis, Mars Climate Database v. 5.1. User Manual, Technical Report, ESTEC Contract, 2014. http://www-mars.lmd.jussieu.fr/mars/info_web/user_manual_5.0.pdf.

[24] F. Forget, F. Hourdin, R. Fournier, C. Hourdin, O. Talagrand, M. Collins, S.R. Lewis, P.L. Read, J.-P. Huot, Improved general circulation models of the martian atmosphere from the surface to above 80 km, J. Geophys. Res.: Planets 104 (E10) (1999) 24155–24175. https://doi.org/10.1029/1999je001025

[25] P. Withers, R. Pratt, An observational study of the response of the upper atmosphere of mars to lower atmospheric dust storms, Icarus 225 (1) (2013) 378–389. https://doi.org/10.1016/j.icarus.2013.02.032

[26] J. Wu, Z. Zhang, A. Hou, M. Zhu, Q. Wang, Nonlinear structural dynamics of the inflatable re-entry vehicle experiment (IRVE), in: 22Nd AIAA International Space Planes and Hypersonics Systems and Technologies Conference, 2018, p. 5204. https://doi.org/10.2514/6.2018-5204

[27] I.-L. Chern, J. Glimm, O. Mcbryan, B. Plohr, S. Yaniv, Front tracking for gas dynamics, J. Comput. Phys. 62 (1) (1986) 83–110. https://doi.org/10.1016/0021-9991(86)90101-4

[28] G. Moretti, Computation of flows with shocks, Annu. Rev. Fluid Mech. 19 (Volume 19, 1987) (1987) 313–337. https://doi.org/10.1146/annurev.fl.19.010187.001525

[29] H. Si, Tetgen, a delaunay-Based quality tetrahedral mesh generator, ACM Trans. Math. Softw. 41 (2) (2015) 11:1–11:36. https://doi.org/10.1145/2629697

[30] A. Assonitis, R. Paciorri, C.F. Ollivier Gooch, A. Bonfiglioli, 3D Flow computations over blunt bodies at hypersonic speeds using shock-fitting technique, in: AIAA Aviation 2022 Forum, 2022, p. 3989. https://doi.org/10.2514/6.2022-3989

[31] A. Bonfiglioli, Fluctuation splitting schemes for the compressible and incompressible euler and navier-Stokes equations, Int. J. Comut. Fluid Dyn. 14 (1) (2000) 21–39. https://doi.org/10.1080/10618560008940713

[32] A. Bonfiglioli, R. Paciorri, A mass-matrix formulation of unsteady fluctuation splitting schemes consistent with Roe's parameter vector, Int. J. Comut. Fluid Dyn. 27 (4–5) (2013) 210 – 227. https://doi.org/10.1080/10618562.2013.813491

[33] MSC Nastran 2023.4 Reference Guide, 2023.

[34] T. Wu, Z. Yuan, K. Jiang, D. Tian, Research on the effectiveness of pressure drag reduction in high mach number flow, Aerosp. Sci. Technol. (2025) 110437.

[35] G. Swanson, B. Smith, R. Akamine, R.J. Bodkin, N. Cheatwood, A.R. Parker, S. Hughes, D. Gaddy, A. Parker, The HIAD orbital flight demonstration instrumentation suite, in: International Planetary Probe Workshop, ARC-E-DAA-TN57454, 2018.

[36] K. Sutton, R.A. Graves, Jr, A general stagnation-point convective heating equation for arbitrary gas mixtures, Technical Report, 1971. https://ntrs.nasa.gov/api/citations/19720003329/downloads/19720003329.pdf.

[37] MatWeb LLC, MatWeb: Online Materials Information Resource, 2025, URL: https://www.matweb.com/search/DataSheet.aspx?MatGUID=99c680bc28dd409fb7e8fd3ddbcee537.

[38] E.H. Hirschel, C. Weiland, Selected aerothermodynamic design problems of hypersonic flight vehicles, 229, Springer Science & Business Media, 2009.

[39] C.D. Karlgaard, R. Deshmukh, S. Dutta, A.M. Korzun, B.R. Hollis, Trajectory reconstruction of the low-Earth orbit flight test of an inflatable decelerator, in: AIAA SciTech 2024 Forum, 2024, p. 1502.

[40] S. Hughes, R. Dillman, B. Starr, R. Stephan, M. Lindell, C. Player, F. Cheatwood, Inflatable re-entry vehicle experiment (IRVE) design overview, in: 18Th AIAA Aerodynamic Decelerator Systems Technology Conference and Seminar, 2005, p. 1636. https://doi.org/10.2514/6.2018-5204

[41] M. Van Der List, L.D. Van Vliet, H.M. Sanders, P. Put, J. Elst, Applications for solid propellant cool gas generator technology, in: 4Th International Spacecraft Propulsion Conference, 555, 2004. https://adsabs.harvard.edu/full/2004ESASP.555E.134V.

[42] K. Gantois, F. Teston, O. Montenbruck, P. Vuilleumier, P. van Braembusche, PROBA-2 Mission and new technologies overview (2006). https://ilrs.cddis.eosdis.nasa.gov/docs/ESA4S_06_11d.pdf.

[43] A. Viquerat, M. Schenk, B. Sanders, V. Lappas, Inflatable rigidisable mast for end-of-life deorbiting system, in: European Conference on Spacecraft Structures, Materials and Environmental Testing (SSMET),Vol. 2014, 2014, pp. 1–10. http://www.markschenk.com/research/files/SSMET2014-InflateSail.pdf.

[44] I.M. Dietlein, G. Guidotti, I. Pontijas Fuentes, F. Trovarelli, A. Rivero Martín, T. Schleutker, S. Callsen, K. Bergmann, C. Julien, Y. Dauvois, et al., Development of inflatable heat shield technology for re-Entry systems in EFESTO project, in: 9Th European Conference for Aeronautics and Space Science, EUCASS 2022, 2022. https://www.eucass.eu/doi/EUCASS2022-7198.pdf.

[45] G. Brown, J. Lingard, M. Darley, J. Underwood, Inflatable aerocapture decelerators for mars orbiters, in: 19Th AIAA Aerodynamic Decelerator Systems Technology Conference and Seminar, 2007, p. 2543. https://doi.org/10.2514/6.2007-2543